Ocean Engineering 289 (2023) 116304

Contents lists available at ScienceDirect

Ocean Engineering

journal homepage: www.elsevier.com/locate/oceaneng

An efficient method of defining the *tail* of a crest height distribution

Chong Huo *, Chris Swan, Ioannis Karmpadakis, Li Ma

Department of Civil and Environmental Engineering, Imperial College London, South Kensington Campus, London SW7 2AZ, UK

ARTICLE INFO

Keywords:
Crest-height statistics
Design crest heights
Short-term extremes
Nonlinear amplifications
Wave breaking

ABSTRACT

The exceedance probability of wave crest elevation is a critical environmental input for the design/re-assessment of marine structures. With attention often focused on structural reliability, and in some cases survivability, the largest wave crests arising at the smallest exceedance probabilities, said to be located in the *tail* of a distribution, are of primary interest. This paper explains why present design practice may be non-conservative in the most extreme seas and outlines a new method by which the *tail* of the distribution can be defined using a relatively small number of deterministic wave events. This avoids the need to explore the entire distribution using very long (and expensive) random wave simulations. The new approach allows both an extension of the distribution to smaller exceedance probabilities and a concentration on the largest most design relevant crest heights. Having demonstrated the success of the proposed method by comparisons to laboratory data, the analysis is extended to include the effective prediction of the associated confidence intervals (CIs). With the highest waves subject to the largest statistical uncertainty, the paper explores the nonlinear changes in CI, demonstrates that these can also be accurately and efficiently defined, and explains how CI may be reduced. The focus of the paper lies in improved design calculations, based upon the nonlinear dynamics of extreme waves in realistic seas.

1. Introduction: crest heights, uncertainty and design requirements

The exceedance probability of wave crest elevation, commonly referred to as a crest height distribution, defines the probability that a wave crest (η_c) exceeds a pre-determined value, $Q(\hat{n_c}) = \text{Prob.}(\eta_c \geq \hat{n_c})$. This is key to the design of all marine structures and is usually defined at a single point (x_0, y_0); the time–history of the water surface elevation denoted by $\eta(x_0, y_0, t)$, the individual wave cycles identified using a zero up-crossing analysis, and the wave crests corresponding to the maximum surface elevation within each cycle. When the data relate to the occurrence of crest heights in a given sea state (the latter defined in terms of a significant wave height, H_s, spectral peak period, T_p, and underlying spectral shape, $S_{\eta\eta}(\omega, \theta)$, where ω is the circular wave frequency and θ the direction of wave propagation) the short-term crest height distribution is defined. If, in contrast, the data relate to all possible sea states at a given location (x_0, y_0), the long-term crest height distribution arises.

When considering the design of a new offshore structure, or the re-assessment of an existing structure, it is the long-term distribution of the applied loading that determines the probability of failure and hence the reliability of the structure. However, in many instances the design codes (ISO, 2013; API, 2014; NORSOK, 2017; DNV-GL, 2019) allow (in some instances encourage) the use of loading recipes based upon highly simplified wave models. Although the appropriateness of this is the subject of on-going debate (see, for example, Ma and Swan, 2023) it allows design criteria to be specified in terms of an n-year wave rather than an n-year load. Whilst the convenience of this is beyond doubt, caution must be exercised to ensure that non-conservatisms are not inadvertently introduced.

In addition to these concerns, it is also important to acknowledge that with design/re-assessment inevitably specified in terms of large events (whether based upon crest heights, wave heights or applied loads) corresponding to small exceedance probabilities, they lie in the so-called *tail* of the distribution. As such, any predicted value will be subject to significant statistical uncertainty. This must be assessed and included if a reliability analysis is to be rigorous.

The present paper will address the short-term distribution of crest heights, outlining a new method to quantify the *tail* of this distribution. The goal is to generate data specific to this task, without the need to generate data appropriate to all exceedance probabilities, but at the same time retaining the ability to define the probabilities to which specific events relate. In seeking to achieve this the purpose of the paper is two-fold:

* Corresponding author.
E-mail addresses: chong.huo15@imperial.ac.uk (C. Huo), c.swan@imperial.ac.uk (C. Swan), i.karmpadakis@imperial.ac.uk (I. Karmpadakis), l.ma@imperial.ac.uk (L. Ma).

https://doi.org/10.1016/j.oceaneng.2023.116304
Received 4 August 2023; Received in revised form 6 October 2023; Accepted 6 November 2023
Available online 15 November 2023

(a) To better understand the nature of the events arising in the *tail* of the distribution, particularly the occurrence of an effective upper-bound to η_c.
(b) To reduce the statistical uncertainty in what is the most uncertain part of the statistical distribution.

Whilst the present paper will stay focused on the short-term crest height distribution, since this is easiest to explore/validate, the method can also be adopted to describe the long-term crest height distribution, provided the distribution of sea states is known or can be inferred. More generally, the method could also be adapted to describe the *tail* of both the short-term and the long-term distribution of loads. These extensions of the present method are the subject of on-going studies and will be reported in subsequent papers.

The paper continues in Section 2 with background information describing the physics that underpins the evolution of the largest crests heights. This is key to the methodology outlined in Section 3; the purpose being to identify the underlying linear wave events that will grow and evolve in a fully nonlinear sense, including the effects of wave breaking, to produce the largest events located in the *tail* of the crest height distribution. In Section 4, the transformation from a linear to a fully nonlinear representation of the selected wave events is addressed. The present paper adopts a laboratory based approach. The advantages and disadvantages of alternative numerical procedures are also discussed. The practical implementation of the new methodology is described in Section 5. This highlights the improved representation that can be achieved, alongside the substantial cost savings (in terms of reduced effort) when compared to traditional, very long, random wave simulations. Section 6 concerns the confidence intervals (CIs), showing the importance of nonlinearities and the success of the present method in predicting the CIs appropriate to the *tail* of the distributions. Finally, the practical implementation of the results, together with potential future developments, are summarised in the concluding remarks given in Section 7.

2. Background: the nonlinear evolution of the highest crests

The simplest model describing the short-term distribution of crest heights is the Rayleigh distribution (Longuet-Higgins, 1952). This is a linear model in which

$$Q(\eta_c) = \exp\left[-8\left(\frac{\eta_c}{H_s}\right)^2\right], \tag{1}$$

where the symbols are as defined previously and H_s is calculated using its spectral definition: $H_s = 4\sqrt{m_0} = 4\sigma_\eta$, where σ_η is the standard deviation of $\eta(t)$ and m_0 the zeroth ($n = 0$) spectral moment based upon

$$m_n = \int_0^\infty f^n S_{\eta\eta}(f)\, df, \tag{2}$$

where f is the frequency or $\omega/2\pi$.

It is well understood that realistic design sea states are not linear, the nonlinear amplification of the largest crest heights ensuring that Eq. (1) is non-conservative for small Q. To begin correcting for this, Forristall (2000) undertook numerical calculations based upon the second-order random or irregular wave theory proposed by Sharma and Dean (1981) and fitted a two-parameter Weibull distribution such that:

$$Q(\eta_c) = \exp\left[-\left(\frac{\eta_c}{\alpha H_s}\right)^\beta\right], \tag{3}$$

where the scale (α) and shape (β) parameters for directionally spread seas are given by

$$\alpha = 0.3536 + 0.2568 S_1 + 0.0800 U_r,$$

$$\beta = 2 - 1.7912 S_1 - 0.5302 U_r + 0.2824 U_r^2. \tag{4}$$

These coefficients are both expressed in terms of the mean sea state steepness, S_1, and the Ursell number, U_r, defined as

$$S_1 = \frac{2\pi H_s}{g T_1^2} \quad \text{and} \quad U_r = \frac{H_s}{k_1^2 d^3}, \tag{5}$$

where T_1 is the mean period defined by m_0/m_1 (using Eq. (2)) and k_1 the wave number corresponding to T_1 calculated using the linear dispersion equation applied in the local water depth, d.

Although Eq. (3) provides a significant improvement over Eq. (1) and is commonly adopted in current design practice (ISO, 2013; API, 2014; NORSOK, 2017; DNV-GL, 2019), this should not distract from the fact that it is based upon a weakly nonlinear, second-order, wave theory. As such, it provides an important but first approximation to the role of nonlinearity. Previous work has shown that when an individual wave becomes increasingly nonlinear, the terms arising at progressively higher orders of wave steepness become increasingly important. Put simply, as an individual wave becomes steeper, more terms are required in a classical (Stokes-type) series expansion to ensure a converged and accurate solution. Numerous researchers have provided evidence of this. In regular waves the limits of validity of the various wave theories (following Dean, 1970, Le Méhauté, 1976 and Sobey et al., 1987) confirm this; whilst in irregular waves the deterministic observations reported by Baldock et al. (1996), Johannessen and Swan (2001, 2003) and Adcock et al. (2015) are equally clear. However inconvenient from an engineering perspective, this behaviour is exactly as expected. Indeed, it represents a fundamental characteristic of all surface water waves; it arises because of the nonlinearity driven by the two free surface boundary conditions. Together, these define both the shape of the wave profile and, most importantly in the present context, the height of the wave crest for a given linear input.

At a fundamental level the nonlinearity of an evolving wave form arises due to a combination of:

(a) The *bound* waves that arise at each successive order of wave steepness, $(a_i k_i)^n$ where $n \geq 2$. At second-order ($n = 2$) these include both the frequency-sum and -difference terms, the relative importance depending on the effective water depth, $k_i d$.
(b) The *near-resonant* interactions involving the growth of new freely propagating wave components leading to local changes in the underlying wave spectrum. These first arise at third-order ($n = 3$), which explain the slow (long-term) evolution of a wave spectrum first noted by Hasselmann (1962), but can also develop more rapidly in the presence of highly nonlinear deterministic wave events (Gibson and Swan, 2007).

Direct evidence of the practical importance of these effects in respect of the crest height distribution was first shown by Latheef and Swan (2013) in deep water and, more recently, by Karmpadakis et al. (2019) in intermediate water depths. In both cases long random wave simulations were undertaken in a highly controlled laboratory environment. Having ensured that the laboratory data was both spatially homogeneous and ergodic, a minimum of twenty 3-hour[1] simulations (or seeds) were generated for a broad range of sea states involving realistic frequency and directional spectra. In each case the concatenated data allowed the crest height distribution to be quantified over a broad range of exceedance probabilities, $Q \geq 10^{-4}$, with the confidence intervals (reflecting the statistical uncertainty) reduced to a realistic minimum.

In comparing this data to both Eqs. (1) and (3), two competing trends became immediately apparent. The first concerns the nonlinear

[1] The '3-hour' duration is the equivalent full-scale value commonly adopted in metocean analysis. With a length-scale of $l_s = 1:100$, the corresponding time-scale is $t_s = 1:10$ based on Froude number similarity. This requires each laboratory simulation (or seed) to be of approximately 18 min duration. Unless otherwise mentioned all data presented within this paper correspond to the full-scale, with experiments performed in this laboratory scale.

amplification of crest heights beyond second-order, as detailed above. The second the dissipative effects of wave breaking. With many of the largest waves sufficiently steep that they exhibit some form of wave breaking, the *tail* of the crest height distribution is defined by the balance between these competing effects.

The physical insights provided by this laboratory data, combined with an extensive analysis of field data (Karmpadakis et al., 2019), led to the development of a new crest height model (Karmpadakis and Swan, 2022). This builds upon Eqs. (1) and (3), incorporating important contributions from Tayfun (2006), Fedele and Tayfun (2009), Fedele et al. (2016, 2019). Following a normalisation by H_s, the non-linear crest height for a given exceedance probability, η_{NL}, was defined by:

$$\xi = \frac{\eta_{\mathrm{NL}}}{H_s} = (\chi + 2\mu\chi^2 + \kappa\mu\chi)(A\chi + B). \tag{6}$$

Considering the first bracket on the right, the terms define the linear, second-order and higher-order contributions respectively. Taking each in turn: $\chi = \eta^{(1)}/H_s$, where $\eta^{(1)}$ is the Rayleigh-distributed crest height from Eq. (1):

$$\eta^{(1)} = \frac{1}{\sqrt{8}} H_s(-\ln Q)^{1/2}. \tag{7}$$

The second term follows Tayfun (1994) and adopts the description of μ given in Tayfun (2006). With (α, β) introduced in Eq. (4) expressed in terms of S_1 and U_r (Eq. (5)), this exactly reproduces the Forristall (2000) model. The third term represents the nonlinear contribution beyond second-order; the functional form of this term being based upon an extensive fitting of the predicted nonlinear crest heights to a combination of experimental and field data recorded in steep, but non-breaking, sea states.

Finally, the second bracket on the right of Eq. (6) describes the dissipative effects of wave breaking: the coefficients A and B, again expressed in terms of S_1 and U_r, fitted to laboratory data describing the crest heights recorded in sea states characterised by extensive wave breaking. Full details of both the fitting process and the success of the model in respect of both independent laboratory data (not used in the model development) and field data are given in Karmpadakis and Swan (2022).

Although the model outlined in Eq. (6) represents an important step forward,[2] the difficulties associated with fitting a model to data involving two competing processes in the *tail* of a distribution, which will inevitable be subject to significant statistical uncertainty, should not be under-estimated. The scarcity of data lies at the heart of this problem. In respect of field data, little can be done except to continue expensive field monitoring programmes and hope that extreme events (both in terms of sea states and individual waves) are successfully recorded. In contrast, more laboratory data involving yet longer random wave simulations can be recorded. However, a substantial reduction in the confidence intervals associated with the *tail* of the distribution requires orders of magnitude more data. Unfortunately this becomes impractical on cost grounds alone. These difficulties can be addressed by the new method outlined in Sections 3 and 4.

Before turning our attention to the new method, it is instructive to consider the evidence supporting the role of wave breaking, to clarify whether it provides an upper bound to η_c in a given sea state and, if not, why not? Fig. 1 shows the non-dimensionalised crest height distribution, $Q(\eta_c/H_s)$, in two directionally spread ($\sigma_\theta = 15°$), relatively deep water ($k_p d = 2.03$) sea states; where σ_θ is the standard deviation of a normally-distributed directional spread and k_p the wave number corresponding to spectral peak. The difference between these cases lies in the sea state steepness: Fig. 1(b) concerning a sea state that is steeper than Fig. 1(a). This data was first presented in Latheef and Swan (2013); the difference being that simultaneous video records of the water surface elevation has enabled the separation of the non-breaking and breaking wave events; the latter including everything from incipient spilling to full over-turning. In both cases the data are compared to the linear Rayleigh distribution (Eq. (1)), Forristall's second-order distribution (Eq. (3)) and the fully nonlinear model (Eq. (6)) by Karmpadakis and Swan (2022). In applying this latter model, the nonlinear amplification has been applied both with and without the dissipative effects of wave breaking. In making these comparisons, several points are immediately apparent:

(a) The nonlinear amplification beyond second-order; much of the data lying above the Forristall prediction.
(b) The dissipative effects of wave breaking in the *tail* of the distribution. This is clearly defined in the steeper sea state (Fig. 1(b)) where the largest crest heights are reduced back towards the second-order predictions. This suggests that in this case the two nonlinear processes (amplification and breaking) almost cancel out at the smallest exceedance probabilities.
(c) To quantify the effects of wave breaking, comparisons should be made between the breaking events (red dots) and the largest model predictions; the latter including nonlinear amplification but not breaking ($A = 0$ and $B = 1.0$ in Eq. (6)).
(d) The agreement between the laboratory data and the full form of Eq. (6) is supportive of the model proposed by Karmpadakis and Swan (2022). Importantly, these data were not used as part of the initial model calibration.

Given the data presented on Fig. 1(b), it is important to ascertain whether the occurrence of wave breaking imposes an upper-bound to η_c/H_s. If this is the case, the *tail* of the crest height distribution simply becomes asymptotic to this limit; the latter defining the appropriate design input. In very shallow (coastal) waters wave breaking is critically dependent upon the local water depth; the relevant limits given by $H_{\max}/d < 0.78$ and $\eta_c/H_{\max} < 1.0$. However, as d increases wave breaking becomes increasingly dependent upon steepness, either $\eta_c k_p$ or $\frac{1}{2} H k_p$, and the occurrence of an effective limit becomes more uncertain. To explore this Fig. 2 presents data (Ma, 2017) relating to a steep (design relevant) sea state in an intermediate water depth ($k_p d = 1.04$). This case was chosen because wave breaking was known to be important (Tychsen et al., 2016), but with $d = 45$ m the individual waves are unlikely to be depth-limited. In considering successive sub-plots, progressively more random seeds are incorporated, the total data base extending to more than 200 × 3-hour simulations of a single sea state. As far as the authors are aware, this is the largest data base relating to a single sea state ever recorded. As such, it is ideally placed to explore the occurrence of an effective upper-bound. In comparing the sub-plots, the inclusion of more data ensures the *tail* of the distribution extends to smaller exceedance probabilities, with reduced confidence intervals; the latter reflecting the sample variability or statistical uncertainty. Most importantly, there are markedly different comparisons to the established solutions. Two trends merit particular attention:

(a) The down-shifting of the data to smaller Q reduces the apparent departures from the second-order model, Eq. (3). This is closely linked to a reduction in the confidence intervals (indicated by the dashed lines) as discussed below.
(b) When all the data is included (Fig. 2(d)) the dissipative effects of wave breaking again appear to counteract the nonlinear amplifications beyond second-order. However, despite the exceptionally long data record and the substantially reduced confidence intervals there is no evidence of an upper-bound, or hard cut-off, in terms of η_c/H_s.

At first sight the absence of an upper-bound appears to be at odds with expectations. However, with wave breaking in deeper waters dependent on the steepness of individual waves and therefore intrinsically

[2] Evidence of this is provided by its application in state-of-the-art design calculations and the recommendations arising from a recent UK HSE review of the integrity of fixed structures subject to extreme environmental loading on the UK continental shelf (Swan and Gibson, 2018).

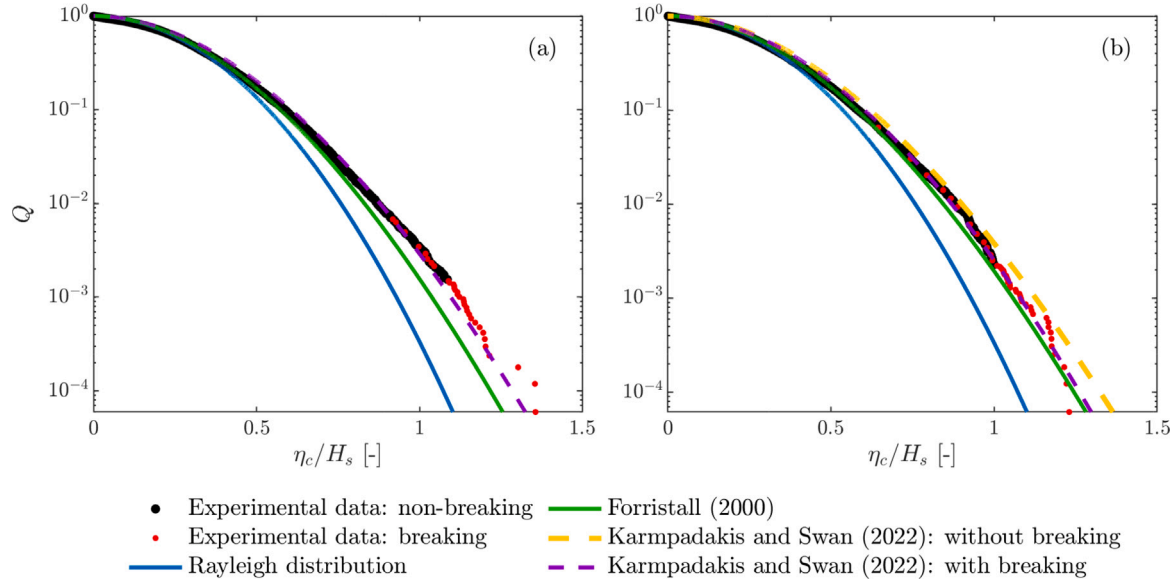

Fig. 1. Normalised crest height distributions $Q(\eta_c/H_s)$, for directionally spread ($\sigma_\theta = 15°$) seas with $T_p = 16$s and (a) $H_s = 15$ m and (b) $H_s = 17.5$ m. Note that the two solutions based upon Karmpadakis and Swan (2022) overlie in (a).

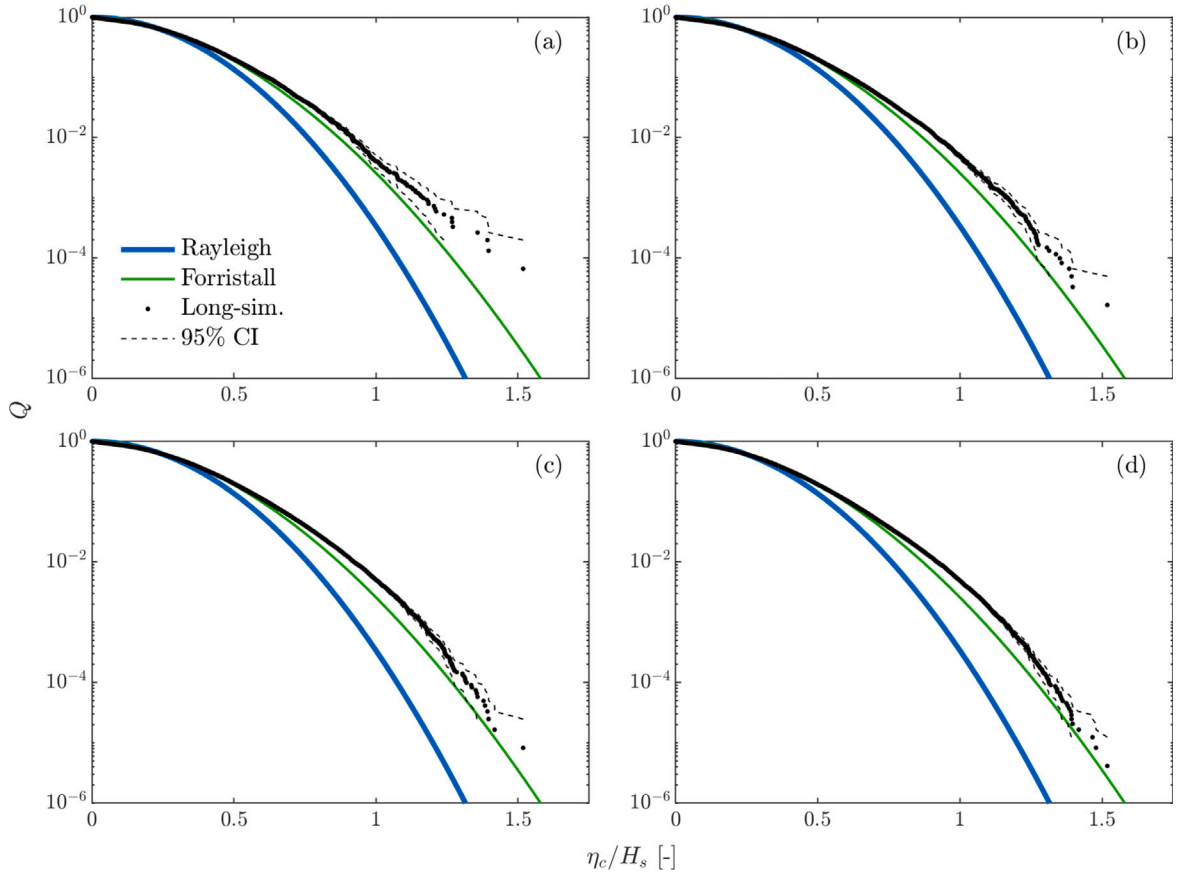

Fig. 2. The effect of sample duration on $Q(\eta_c/H_s)$. (a) 20 × 3-hour sea states, (b) 80 × 3-hour, (c) 160 × 3-hour, (d) 320 × 3-hour. The data (Long-sim.) are shown alongside their 95% confidence intervals (95% CI).

linked to the local wave period, the random variation in the latter (Fig. 3) provides a possible explanation. Within Fig. 3 the individual wave periods are normalised by the trough-to-trough period, T_{tt}, of the quasi-deterministic (QD) focused wave. This defines the most probable shape of a large linear wave, given the underlying wave spectrum, $S_{\eta\eta}(\omega, \theta)$, and is based upon the theory of Lindgren (1970), Boccotti (1983) and Phillips et al. (1993a and 1993b). However, the variability in the period of the largest waves (±10%), ensures that no upper-bound applies: a large wave with an increased period being less steep and therefore less susceptible to the dissipative effects of wave breaking.

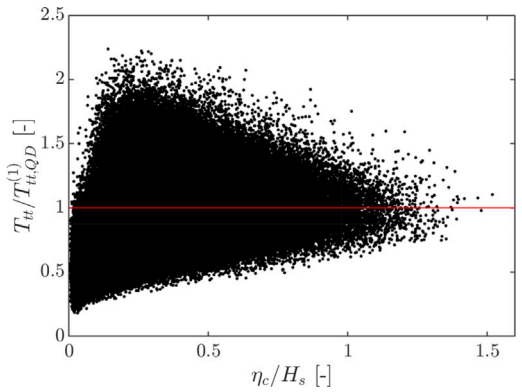

Fig. 3. Scatter plot of normalised crest heights, η_c/H_s, and their associated trough-to-trough wave periods, T_{tt}, normalised by the corresponding period of a QD (focused) wave, $T^{(1)}_{tt,QD}$.

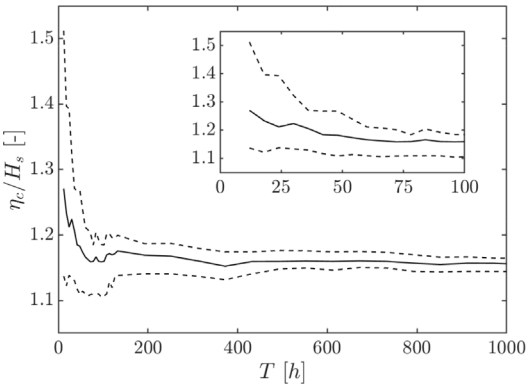

Fig. 4. Reduction in 95% confidence intervals at $Q = 10^{-3}$ with increasing sample duration (T in hours). All data relates to the sea state considered in Figs. 2 and 3 with $H_s = 16.7$ m, $T_p = 17.7$ s and $k_p d = 1.04$. The inset provides a zoomed-in view of the initial 0-to −100-hour interval.

Fig. 4 concerns the reduced statistical variability, indicated by the 95% confidence intervals, that arise with increasing data. These estimates are based upon an exceedance probability of $Q = 10^{-3}$, calculated using established bootstrap techniques (Efron, 1979) applied to the long random simulations outlined in Fig. 2. The key point is that the inclusion of more data inevitably leads to a narrowing of the confidence intervals, but the 'law of diminishing returns' clearly applies; a prohibitively large amount of data being required to realise any subsequent reduction. To put this figure into perspective, most commercial model testing is typically undertaken using 5 (or less) 3-hour random seeds. Indeed, outside research studies or joint industry projects, the largest number of seeds investigated would be of order 20. Clearly, even with this number, the confidence limits remain substantial, and *tail* of the distribution poorly defined.

3. Methodology

In seeking an efficient and accurate description of the *tail* of a crest height distribution, we must first consider the origins of the largest waves arising in realistic seas that are broad-banded in both frequency and direction. The challenge is to pre-determine those wave events that could, potentially, become very large and to transform these waves into the *tail* of the distribution without the burden of generating or calculating all possible wave events. Whilst much has been written about the importance of modulational instabilities, such as Benjamin-Feir type instabilities (Benjamin and Feir, 1967), in the development of so-called rogue waves (for example, Janssen, 2003, Kharif and Pelinovsky, 2003 and Chabchoub et al., 2011), these only tend to dominate in sea states that are narrow-banded in frequency and uni-directional. Since realistic sea states, particularly severe sea states, are broad-banded in both frequency and direction, the constructive interference of freely propagating (mostly linear) wave components due to both frequency and directional dispersion will dominate in deep water. That is not to underestimate the importance of the *bound* and *near-resonant* nonlinearities, nor the dissipative effects of wave breaking (Section 2). As such, if a wave is to potentially contribute to the low probability *tail* of the crest height distribution at a given point, it must first begin to evolve as a large linear wave, with the superposition of energy in both space and time. Whilst these arguments are, in-part, consistent with the quasi-deterministic (QD) focused waves studied by Lindgren (1970), Boccotti (1983) and Phillips et al. (1993a and 1993b), we are not suggesting that the underlying linear wave components will be perfectly focused, rather that there must be a degree of focusing, particularly around the spectral peak. Moreover, we are certainly not assuming that the most probable shape of a large linear wave provides the basis for all large nonlinear waves that populate the *tail* of $Q(\eta_c)$. Indeed, the notion of a most probable wave shape associated with the maximum (or extreme) η_c is to neglect the inherent variability that is fundamental to the description of the tail. That said, the physics that underpins QD focused waves allows important insights into the nature of the largest waves (see, for example, Karmpadakis and Swan, 2020) and is key to the methodology described below.

When a large nonlinear wave evolves, the near-resonant interactions ensure that it shifts in both space and time. This occurs in both nonlinear random seas, relative to the equivalent (phase-related) linear prediction, and QD focused waves. An example of the latter is given in Fig. 5. This concerns four wave events with increasing linear amplitude sum $A = \sum a_n$, where a_n is the amplitude of the nth frequency component. The larger A, the more nonlinear the wave event and the greater the downstream shifting in space and time. In the left column comparisons are provided between the linear predictions and fully nonlinear laboratory observations at the linear focus position ($x = 0$). In the right column similar comparisons are made at the position of the largest nonlinear crest, the latter denoted by $x^{\mathrm{NL}}_{\max}$. Another way to demonstrate this shift is to consider the spatial envelope of η_c for increasing A (Fig. 6). In this example, the linear focus position is again set to $x = 0$ and all of the data relate to non-breaking waves observed in the laboratory. With increasing A, the downstream shifting of $\eta_c^{\max}$ is clearly defined. In addition, the envelopes become increasingly asymmetric; the wave events focusing more rapidly and de-focusing more slowly. This defines a nonlinear phase-locking in which large waves maintain their amplified crest heights longer than linear calculations predict. This will inevitably alter the *tail* of the crest height distribution.

In seeking to pre-determine the linear wave events that will go on to populate the *tail* of $Q(\eta_c)$, the two effects noted above (downstream shifting and phase locking) must be included. This is achieved by adopting the following steps:

(i) If (x, y, z) define the usual cartesian coordinates in which (x, y) describe a horizontal plane with z measured vertically upwards from the mean water level (MWL) and x is aligned with the main wave direction, then $Q(\eta_c)$ is to be defined at a single point, arbitrarily chosen at $(x, y) = (x_0, y_0)$. As a first step, linear calculations of the desired sea state are made in space and time, $\eta(x, y, t)$. The spatial domain covering an area $(\Delta x \times \Delta y)$ such that:

$$x \in [x_0 - \Delta x, x_0] \quad \text{and}$$

$$y \in [y_0 - \Delta y/2, y_0 + \Delta y/2] \tag{8}$$

and t covering the full duration of the random sample. At this stage no attempt is made to specify Δx and Δy other than to note that they must be sufficiently large to accommodate any

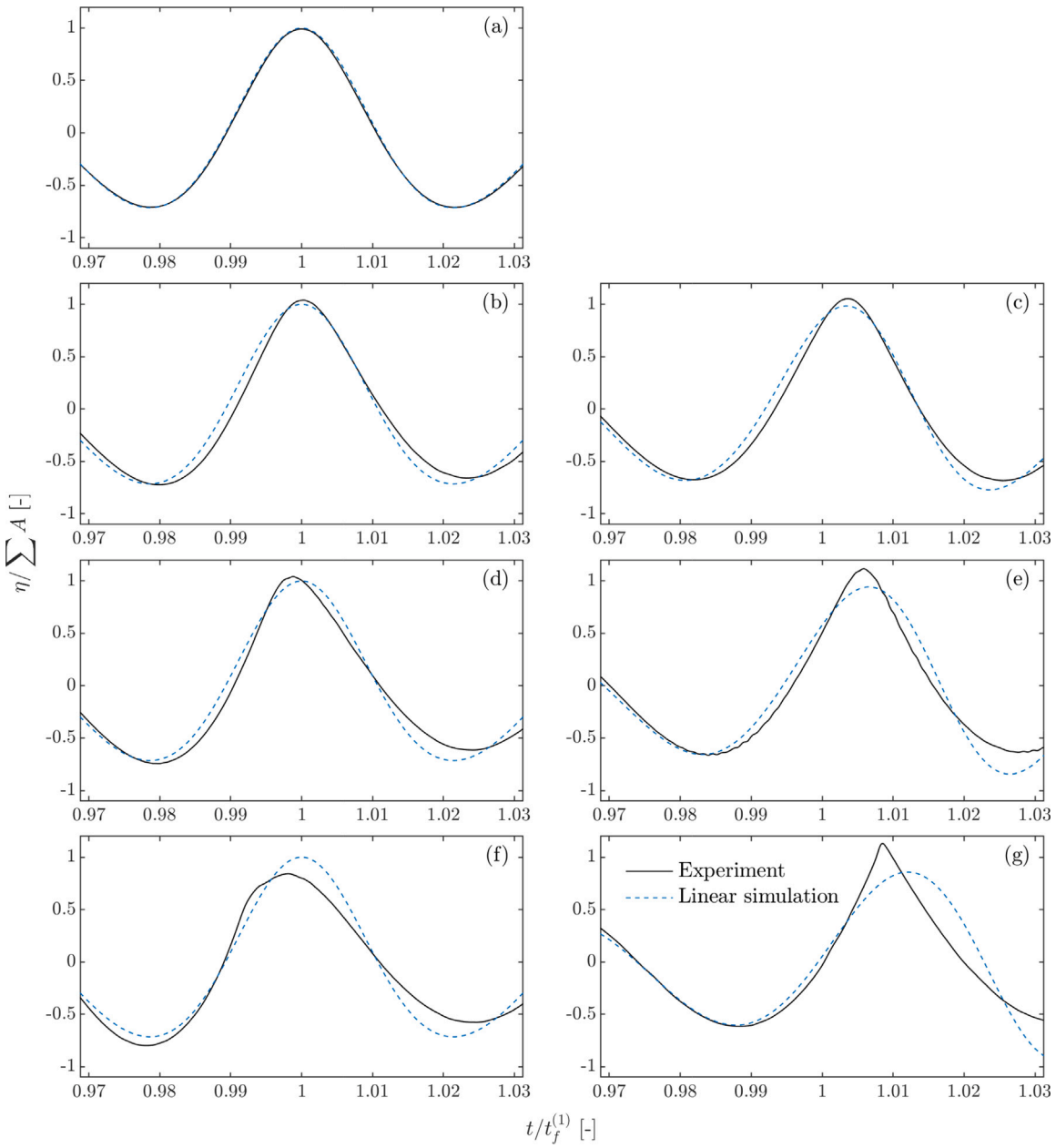

Fig. 5. Downstream shifting of a QD focused wave event with increasing nonlinearity, or input amplitude sum, A. From top to bottom $A = \sum a_n = 0.03,\ 0.08,\ 0.12$ and 0.18 m with the left column at the linearly predicted focus ($x = 0$) and the right column at the position of the largest nonlinear crest height $x_f = 0.2,\ 0.4$ and 0.7 m respectively. The linear focus time $t_f^{(1)} = 32$ s is common for all sub-figures. Note: all of the data is given at laboratory scale.

nonlinear shift in the location of the largest wave events (the appropriate choices of these parameters will be discussed in Section 5). Importantly, the linear calculations outlined above must be based upon the amplitudes (a_n) and phases (ψ_n) of the underlying linear components, both defined randomly in accordance with accepted practice (Tucker and Pitt, 2001).

(ii) Based upon these calculations, all large linear wave events occurring within the pre-determined spatial domain (Eq. (8)) were identified. These are best represented by spatial plots, $\eta(x, y)$, at all relevant times; the four sub-plots given on Fig. 7 showing $\eta(x, y)$ at four times during the evolution of a large wave.

(iii) To rank these events spatial profiles, $\eta(x)$ were extracted for closely-spaced and constant y. An example of this data, at one instant in time, is presented on Fig. 8(a); the maximum surface elevation on each profile noted by a asterisk. By repeating this process for closely-spaced intervals in time, the envelope of the maximum surface elevation describing the evolution of an individual wave event over the entire spatial domain can be defined (Fig. 8(b)). The maximum of this envelope, defining the maximum water surface elevation associated with each individual wave event anywhere over the spatial domain, $\eta^A_{\max}$, is then used to rank the events; the top ranked event having the highest linearly predicted crest elevation irrespective of where it occurs across the pre-determined spatial domain (Eq. (8)).

The calculations outlined in (i), (ii) and (iii) above are entirely linear. As such, they can be undertaken very rapidly. Indeed, the only challenge lies in ensuring that each envelope defines the evolution of a single (individual) wave event. If this is not the case, easily identifiable discontinuities will appear in the location of the maxima (Fig. 8(a)) as a second (larger) wave crest enters the domain.

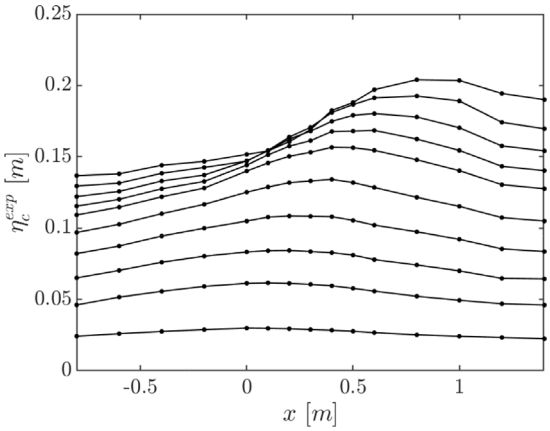

Fig. 6. Envelope of experimentally measured η_c for QD focused wave events with increasing nonlinearity or input amplitude sum, A. Ten cases with A lying in the range 0.03 m $\leq A \leq$ 0.18 m; all relating to non-breaking waves with $T_p = 1.6$ s and $k_p d = 2.03$. Note: all of the data is given at laboratory scale.

To validate the above noted approach, direct comparisons can be made to existing laboratory data involving 40 × 3-hour random simulations (or seeds) of a single sea state. All of the data employed herein was generated in a directional wave basin located in the Hydrodynamics Laboratory in the Civil Engineering Department at Imperial College London. Full details of this facility, the methods of wave generation and the instrumentation employed are given in Latheef and Swan (2013), Latheef et al. (2017) and Karmpadakis et al. (2019). Before presenting these data it is important to note that previous laboratory wave studies undertaken at Imperial College are particularly suited to this task. This will not be the case for all laboratory generated wave data. The reason for this lies in our rigorous application of a theoretical wave paddle calibration (Spinneken and Swan, 2009a,b). The purpose of this is to be confident that we have correctly generated the desired underlying linear wave components. This includes their frequency (ω_n), amplitude (a_n), phase (ψ_n), and direction of propagation (θ_n). The background to this lies in the early generation of QD focused waves: Baldock et al. (1996), Johannessen and Swan (2001, 2003), with the same methods being subsequently applied to long random simulations (Latheef and Swan, 2013, Karmpadakis et al., 2019 and Karmpadakis and Swan, 2020). Moreover, in respect of directionally spread seas a random directional method (RDM) has been applied such that any one frequency component is only generated in one direction to maintain the ergodicity of the target sea state. Once again, this method relies heavily on the accurate generation of the underlying linear components; the benefits are highlighted in Latheef et al. (2017). In adopting these approaches no attempt is made to calibrate or re-scale the measured spectrum to optimise the fit to the target; this simply becomes unnecessary. Unfortunately, these approaches are not always applied; a greater emphasis being placed on the agreement between the measured and target spectrum, even if there are sound physical reasons (nonlinearity, breaking and unwanted wave reflections) why they might differ. In such cases, commonly referred to as a *wave basin calibration*, the accuracy of the underlying linear components is unclear.

Although this distinction is subtle, it is fundamental to the success of the present procedure; the linear calculations outlined in (i), (ii) and (iii) above being directly related to the linear wave components underpinning the fully nonlinear random simulations undertaken in the laboratory. Indeed, the inputs appropriate for the linear calculations ($\omega_n, a_n, \psi_n, \theta_n$) are exactly those sent to the wave paddles. Fig. 9 examines the success of the proposed methodology. In this example the sea state is defined by $H_s = 15$ m, $T_p = 16$ s, $S_{\eta\eta}(\omega)$ is a JONSWAP spectrum with a peak-enhancement factor of $\gamma = 2.5$ and directionality defined by the standard deviation of a frequency-independent wrapped normal distribution, $\sigma_\theta = 20°$. In the linear simulations $\Delta x = 0.25\lambda_p$ and $\Delta y = 0.10\lambda_p$, where λ_p is the wave length of the spectral peak frequency, and the highest 300 wave events were identified from the linear simulation (part (iii)). Given that the inputs defining the laboratory simulations and the linear calculations were identical, the nonlinear crest elevations corresponding to each of these 300 pre-selected linear wave events can be identified from the more than 10,000 wave events generated in the long random records covering 40×3-hour of experimental data. Plotting the nonlinear crest heights at (x_0, y_0) of the 300 largest linear events assuming that they do indeed represent the 300 largest nonlinear events and maintaining the ranking based upon the linearly predicted crest heights give the results presented on Fig. 9(a). All that can be concluded from this figure is that whilst many of the large linear events do, indeed, produce large nonlinear events, the linearly predicted ranking bears no relationship to the actual nonlinear ranking. This is exactly as expected since both the extent of any nonlinear amplification and the dissipative effects of wave breaking are dependent upon the individual wave steepness and this has been completely neglected. However, if the nonlinear crests associated with the 300 large linear events are re-ranked based upon their nonlinear crest heights, Fig. 9(b) shows that the *tail* of the crest height distribution can be accurately defined based upon a limited number (300) of deterministic wave events, the latter selected based upon linear criteria.

In considering this result, two important points should be noted:

(a) Not all the large linear events correspond to large nonlinear events. However, provided both the domain size ($\Delta x, \Delta y$) and the number of linear events considered (N) are sufficiently large, all the large nonlinear events will be captured. As such, the *tail* of the crest height distribution can be defined.

(b) The methodology outlined above only becomes useful (predictive) if individual linear events can be transformed to their nonlinear equivalent. This must include both nonlinear amplification and the dissipative effects of wave breaking. In Fig. 9(b) this transformation was known in advance because the individual events could be identified within the equivalent fully nonlinear long random simulations that had already been undertaken. Clearly the results presented in Fig. 9(b) are important, but not yet predictive.

4. Linear to nonlinear transformation: a laboratory approach

The task that now remains is to define how the pre-determined linear events evolve nonlinearly; specifically the maximum crest elevation that arises at (x_0, y_0). There are two possible approaches to this problem: deterministic laboratory observations and direct numerical calculations. If the problem only involves the nonlinear amplification of a potential flow problem, the latter approach would be preferable. However, with a focus on the *tail* of $Q(\eta_c)$ and having demonstrated the importance of wave breaking, doubt remains whether exact numerical calculations are either possible or practical. Indeed, whilst significant steps have been made in the modelling of individual breaking waves (for example, Jacobsen et al., 2012), the present analysis would require calculations to be extended through the breaking process and to assess the extent to which an earlier breaking wave influences the evolution of a subsequent higher wave; this particularly relates to the downshifting of energy in the frequency domain. Given these difficulties, the present paper will adopt a laboratory approach in which the pre-determined linear events are rapidly generated as a sequence of deterministic waves and the required non-linear crest heights (at (x_0, y_0)) directly recorded. Key to the success of this approach is the ability to consistently reproduce short segments of a measured long random wave record. This is addressed in Fig. 10, within which sub-plot 10(a) considers a large non-breaking wave and 10(b) a very large breaking wave. In both cases comparisons are provided between the wave event recorded as part of the long random wave simulation and two repeated generations of

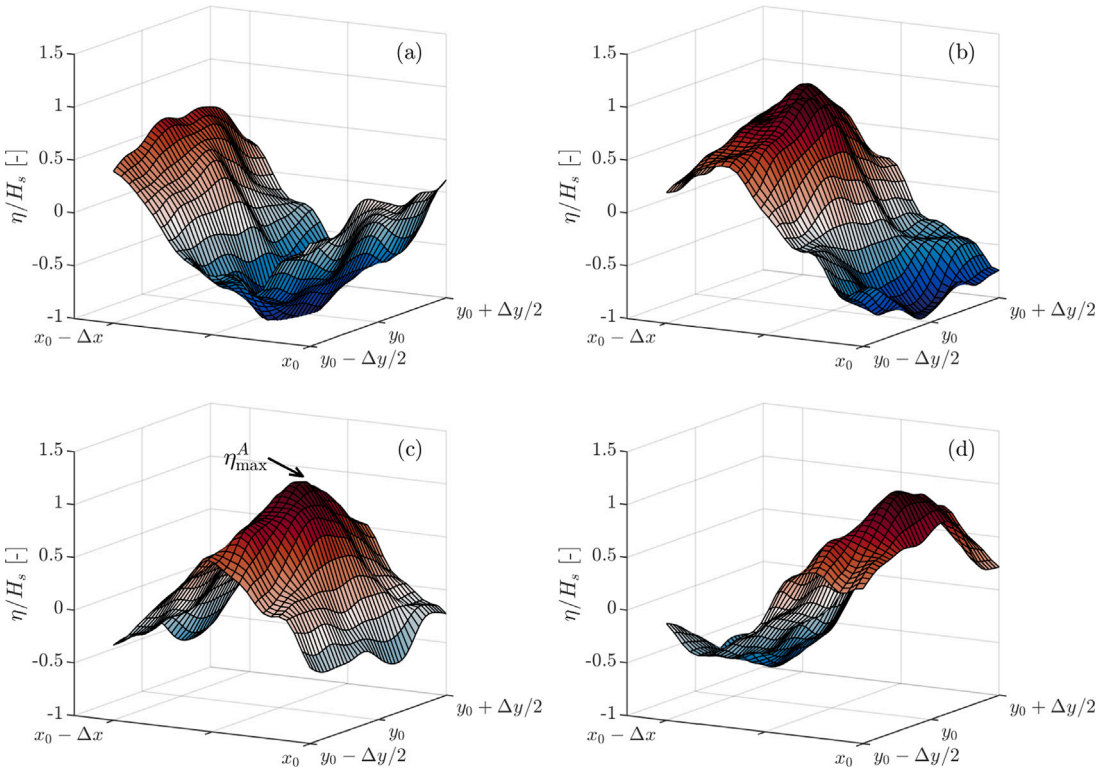

Fig. 7. Spatial profile of the linearly predicted surface elevation, $\eta(x, y)$, at four times: (a) $t = 0$ s, (b) $t = 2.3$ s, (c) $t = 4.7$ s, (d) $t = 7.0$ s This shows the evolution of a large wave event over the domain of interest. Data relates to a sea state with $T_p = 16$ s and $k_p d = 2.03$. In (c), $\eta^A_{\max}$ denotes the maximum elevation of this wave event.

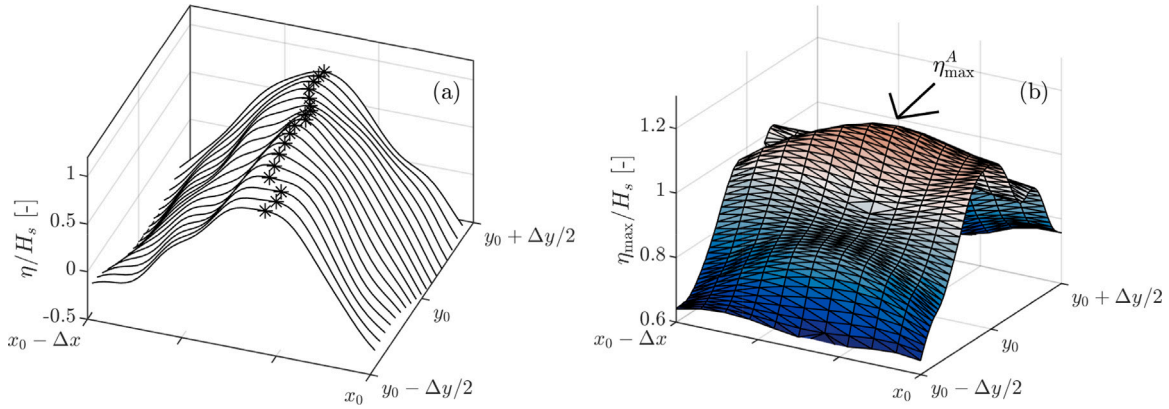

Fig. 8. The generation of a spatial wave envelope. (a) $\eta(x)$ on lines of constant y for one t, with the highest crest elevation marked by [∗]. (b) After repeating (a) for all times relevant to an individual wave event, the envelope of the crest defines $\eta_{\max}(x, y)$ irrespective of the time at which it occurs. The maximum of the envelope, $\eta^A_{\max}$, irrespective of where it occurs within the pre-determined domain is then used to rank the event, allowing the N largest events to be identified. All calculations are based on linear simulations.

a short segment of the wave record centred about the required wave event. Details of how this is achieved are given below; at this point the purpose of Fig. 10 is to establish that any individual wave event within a long random record can be isolated and reproduced as a deterministic event within a short segment of the original; the segment based upon identical linear inputs to the wave paddles. To generate a sequence of large deterministic wave events, whilst maintaining the accuracy noted in Fig. 10, the experimental parameters noted in Table 1 must be optimally defined. If any of these individual times is too small, the accuracy may be reduced. Likewise, if the times are too long the efficiency of their generation will decline.

Given the importance of these parameters to the success of the proposed method, an initial investigation considered the generation of the 20 largest waves recorded in 40 × 3-hour simulations of a sea state defined by $H_s = 10$ m, $T_p = 16$ s, $\gamma = 2.5$ and $\sigma_\theta = 20°$. In this case, the wave events corresponding to the 20 largest were known in advance (from long random simulations) so it was simply a matter of reproducing the same 20 events, within short segments, calculating the average error in the recorded crest heights and assessing how this varied with the chosen parameters (Table 1). This allowed a rapid investigation over a broad range of parameters. Having completed this, a second assessment was undertaken in which all of the wave events with exceedance probabilities lying in the range $10^{-3} \geq Q \geq 10^{-4}$ were generated as deterministic events and the root-mean-square percentage error (RMSPE) between the crest heights recorded in the random and deterministic simulations calculated. This assessment, again undertaken for the sea state noted above, was more onerous in terms of the wave events generated and hence applied to a reduced range of parameters (Table 1). However, it has the benefit of directly quantifying the errors describing the *tail* of $Q(\eta_c)$. Data arising from this second approach is

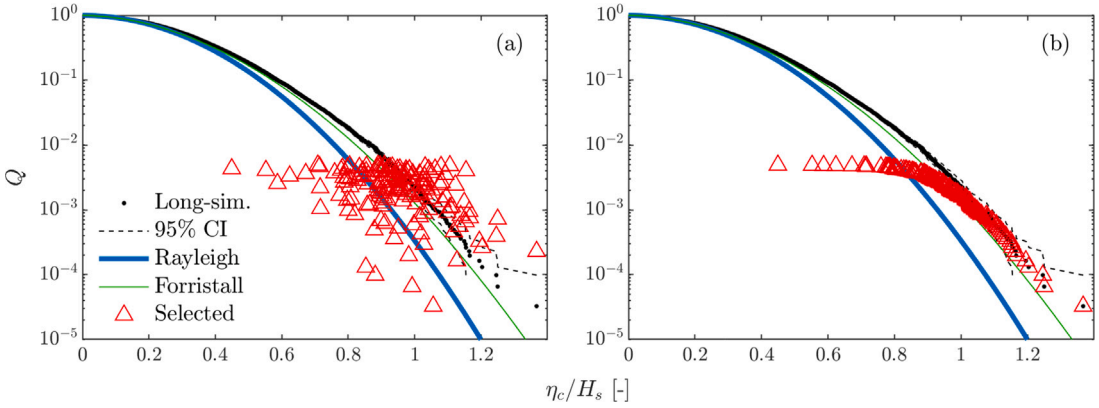

Fig. 9. Analysis of the $N = 300$ wave events selected from a linear simulation (Fig. 8); (a) with the ranking based upon the linearly predicted envelope maximum $\eta^A_{\max}$ and (b) with the data re-ranked. Note that in both sub-figures the nonlinear crest elevation for the event in question is extracted from the relevant section of the long random laboratory simulation.

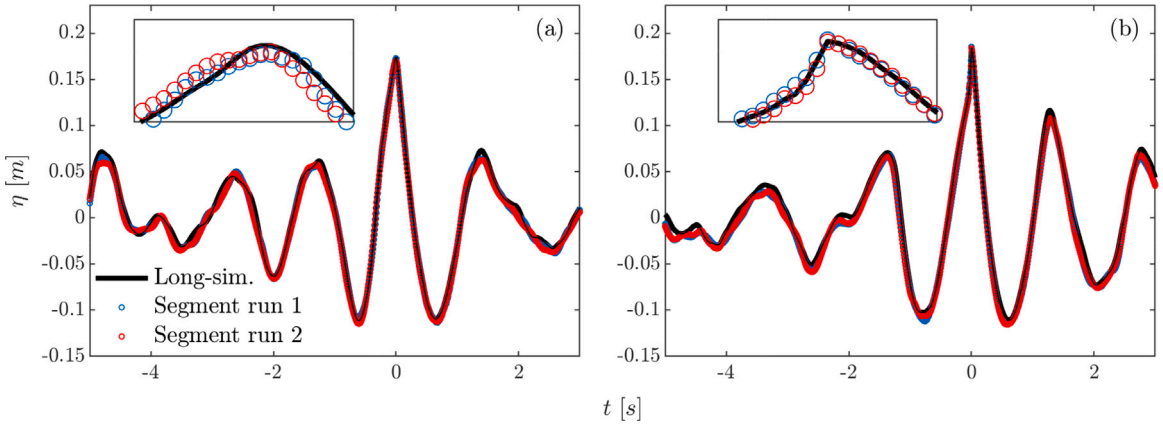

Fig. 10. Reproducing individual events from a long random laboratory simulation of a given sea state ($H_s = 15$ m, $T_p = 16$ s, $\gamma = 2.5$, $\sigma_\theta = 20°$ and $k_p d = 2.03$); comparison between $\eta(t)$ recorded in the full random simulation and the isolated events generated from short segments for (a) a non-breaking wave and (b) a breaking wave.

Table 1
Key parameters when seeking to reproduce large highly nonlinear wave events within short segments of wave records.

Parameter	Definition/Purpose
$t_{\text{pre-run}}$	The duration of paddle operation before the desired wave event occurs at (x_0, y_0). This must be sufficiently long to ensure that all the contributing wave frequencies can propagate from the paddles to (x_0, y_0)
t_{after}	The duration of paddle operation after the desired wave event occurs at (x_0, y_0). Seemingly unimportant but acts in conjunction with the ramp-down (see below) to avoid spurious waves generated by rapid shutdown of the paddles.
$t_{\text{ramp-up}}$, $t_{\text{ramp-down}}$	The intervals over which specified paddle motions are linearly increased (or reduced) at the beginning (or end) of each generating segment. Necessary to avoid abrupt motions of the paddles.
t_{wait}	The period of rest (no wave generation) between adjacent wave generations; after ramp-down and before the next ramp-up. Necessary to avoid build-up of disturbances in the wave basin.

presented on Fig. 11. Based upon these results the chosen parameters were defined as $t_{\text{pre-run}} = 45$ s, $t_{\text{after}} = 5$ s, $t_{\text{ramp-up}} = t_{\text{ramp-down}} = 4$ s and $t_{\text{wait}} = 5$ s. Adopting these values each deterministic segment takes just under a minute to complete, with the next segment commencing 5s after the completion of the last. Most importantly, the data indicates that the RMSPE in the deterministic simulation of the *tail* of $Q(\eta_c)$ is consistently less than 1%.

At this point it is important to discuss the earlier work of Schubert et al. (2020). Whilst there are clearly some similarities between what is presently proposed and what they did, there are also fundamental differences. First, Schubert et al. sought to define the distribution of both the hourly maximum crest heights and wave heights. This was initially achieved using long random laboratory testing. To ensure the most extreme events are included and to reduce the uncertainties associated with the estimated distributions they also used what they call *numerical pre-selection* based upon second-order random wave theory. This model is only weakly nonlinear and, as such, does not incorporate the *near-resonant* wave interactions defining both the *downstream shifting* and the *phase-locking* discussed earlier, nor does it incorporate the dissipative effects of wave breaking. This is not a problem provided a large number of potential wave events are explored (in our case N) arising over a substantial area upstream of the point of interest (in our case $(\Delta x, \Delta y)$). Unfortunately, Schubert et al. did not do this; their numerical pre-selection involved looking at a single point

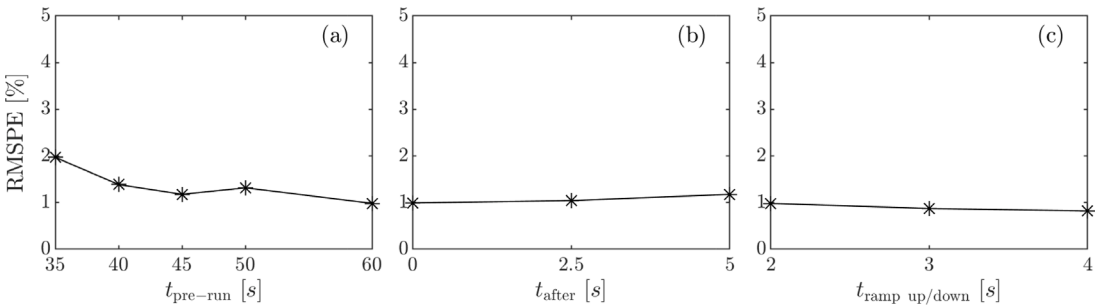

Fig. 11. Defining the optimal choice of running parameters when seeking to reproduce large highly nonlinear wave events within short segments of wave records. Data based upon $N = 300$ wave events recorded in a sea state with $H_s = 10$ m, $T_p = 16$ s, $\gamma = 2.5$, $\sigma_\theta = 20°$ and $k_p d = 2.03$. The error is defined as a Root-Mean-Square percentage (RMSPE) for events lying in the range $10^{-3} \geq Q \geq 10^{-4}$ and used to quantify (a) $t_{\text{pre-run}}$, (b) t_{after}, (c) $t_{\text{ramp-up}}$ and $t_{\text{ramp-down}}$.

(their so-called reference gauge) and they only considered the hourly maximum events arising from long numerical simulations. When taken together, these omissions will produce a non-conservative bias in the estimated parameters. This bias is acknowledged in their paper, the return periods re-estimated using a correction or calibration factor based upon a stochastic analysis of the data arising from their (inappropriate) numerical pre-selection. However, they provide no discussion of the physical cause of this bias and its statistical treatment adds unnecessary uncertainty in the estimated parameters. In contrast, the present approach avoids these shortcomings by explicitly incorporating the physical processes arising from both nonlinear wave evolution and wave breaking in a consistent and robust methodology.

5. Comparisons to available data

Before combining and applying the methods outlined in Sections Section 3 and 4, two additional issues need to be addressed. The first relates to the method explained in Section 3: the identification of the linear events that may, after their nonlinear evolution, populate the *tail* of $Q(\eta_c)$. Specifically, the most appropriate choice of Δx, Δy and N. In Section 3 it was simply assumed that adopting $\Delta x = 0.25\lambda_p$ and $\Delta y = 0.10\lambda_p$ with $N = 300$ was adequate. Having explained how best to quantify the errors in respect to the laboratory parameters (Table 1 and Fig. 11), a similar approach is adopted in terms of Δx, Δy and N in Fig. 12(a), 12(b) and 12(c) respectively. In Figs. 12(a) and 12(b), the data all arise from 40 × 3-hour random wave simulations: N is held constant, the interrogation area is increased (first Δx and then Δy, independently) and the linear wave events identified as described in Section 3. For each linear event the corresponding nonlinear crest elevation arising at (x_0, y_0) was identified from the long random experimental records and the data re-ranked to approximate the *tail* of the distribution. The RMSPEs (relative to the full distribution solely based upon the random experimental data) were then calculated for $10^{-3} \geq Q \geq 10^{-4}$. The variation in the RMSPEs can be explained as follows. The minimum errors occur for $\Delta x = 0.25\lambda_p$ and $\Delta y = 0.10\lambda_p$, hence the chosen values. With reductions in Δx or Δy the RMSPEs increase (particularly with Δx) because not all the relevant large linear events are identified. Likewise, with an increase in Δx or Δy the RMSPEs again increase (particularly with Δy). In this case more linear maxima will potentially occur and N would need to be increased to ensure all the relevant nonlinear maxima at (x_0, y_0) are included. Fig. 12(c) specifically addresses the convergence with N, assuming Δx and Δy are set to the above noted values. Within this figure, the solid line is based upon the identification of specific linearly predicted wave events within the long random data, exactly as described above and in Section 3. Based upon these results there appears little benefit of setting $N > 200$; the RMSPE for $10^{-3} \geq Q \geq 10^{-4}$ having reduced to a very small value (< 1%). In contrast, the dashed line on Fig. 12(c) combines the methods outlined in Sections 3 and 4. Having identified the appropriate linear events, these were re-generated as deterministic segments using the parameters outlined in Section 4 (Table 1). The fact that this almost exactly reproduces the earlier result confirms success of laboratory transformations outlined in Section 4; convergence again being achieved for $N = 200$.

The final point that needs to be addressed concerns the exceedance probabilities that are attributed to individual events. In the preceding plots these were defined by the number of waves arising in the long random wave simulations. If the method is to be truly predictive, it must be applied without prior knowledge arising from long random simulations. In such cases the total number of waves within a simulation must be based upon linear calculations. Whilst this is not expected to change due to nonlinear amplification, the role of wave breaking is less clear. Fig. 13 addresses exactly this point; it considers a broad range of sea state steepnesses and contrasts the total number of waves (Fig. 13(a)) and the corresponding smallest Q (Fig. 13(b)) observed in long random simulations and linear calculations for varying number of seeds, each 3-hour in duration. To be consistent with the usual presentation of $Q(\eta_c)$, the vertical axis of Fig. 13(b) is logarithmic. Whilst the actual Q values are not identical, the difference is very small (< 1.4%); for all practical purposes insignificant when considered on Fig. 13(b). This remains true even when considering the smallest probabilities in the steepest sea states.

Having defined all the necessary parameters, Figs. 14 and 15 combine the methods outlined in Sections 3 and 4 to provide predictions of $Q(\eta_c/H_s)$ for exceedance probabilities lying in the range $10^{-3} \geq Q \geq 10^{-4}$. All of the cases relate to steep sea states defined by $H_s = 15.0$ m, $T_p = 16$ s and $k_p d = 2.03$. This is close to commonly applied 10^{-4} design conditions in the northern North Sea; the steepness of the sea states being such that the *tail* of $Q(\eta_c)$ is substantially affected by wave breaking. Fig. 14 considers three sea states with varying spectral bandwidths; the peak enhancement factor (γ) of the JONSWAP spectrum varying from $\gamma = 1.0$, 2.5 and 5.0 in sub-plots (a), (b) and (c) respectively. Likewise, Fig. 15 considers three sea states with varying directional spreads: $\sigma_\theta = 0°$, 10° and 20°. The first of these examples is uni-directional and therefore physically unrealistic, but the range of directional spreads, $0° < \sigma_\theta \leq 20°$, is consistent with field observations and recommended design guidance for temperate latitudes.[3] In making these comparisons the 40 × 3-hour of random wave data recorded in each case were not in any way used in the predictive approach; it simply provided a means of checking the final result.

Based upon these six cases, it is clear that the *tail* of the crest height distribution can be accurately and very efficiently defined using the method described. To complete 40 × 3-hour random simulations at a scale of $l_s = 1 : 100$ (the corresponding time scale being $t_s = 1 : 10$) takes approximately 20 h of continuous wave basin usage. Full details of how this is achieved is given in Latheef and Swan (2013) and

[3] Although larger directional spreads are observed in hurricanes and tropical cyclones, the present approach remains equally valid.

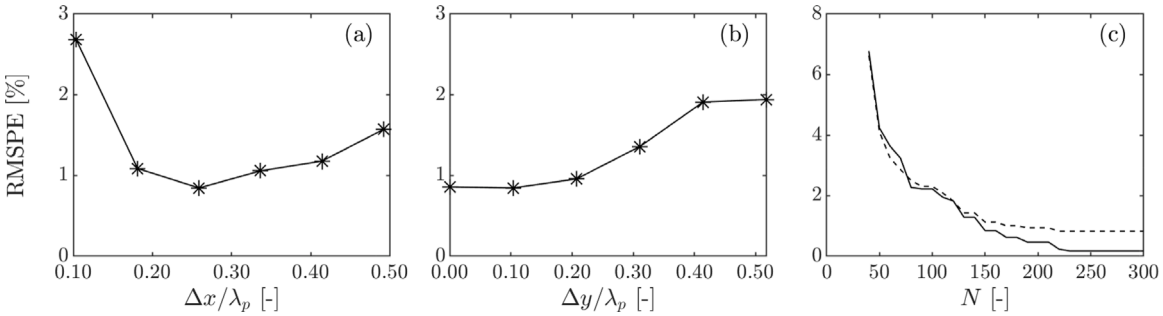

Fig. 12. Optimising the choice of (a) Δx, (b) Δy and (c) N; data again based upon wave events recorded in a sea state with $H_s = 15$ m, $T_p = 16$ s and $k_p d = 2.03$, and the RMSPEs are defined for events lying in the range $10^{-3} \geq Q \geq 10^{-4}$. In part (c) additional comparisons are made between the corresponding wave records identified in the long random simulation [solid line] and results of the short deterministic segments [dash line].

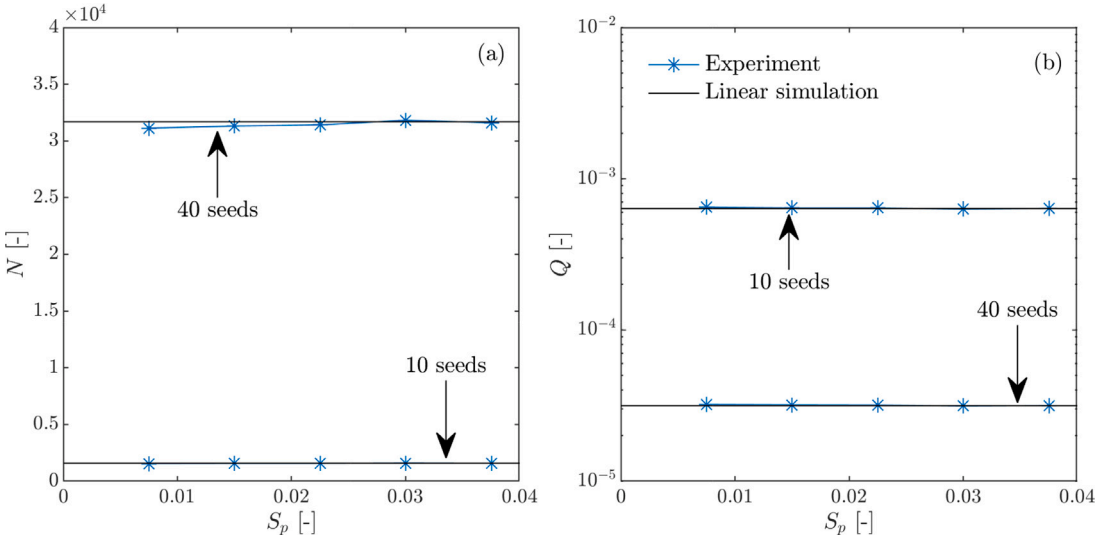

Fig. 13. Comparisons between the number of waves (N) and the smallest corresponding exceedance probability, depending on the number of seeds and the sea state steepness, S_p.

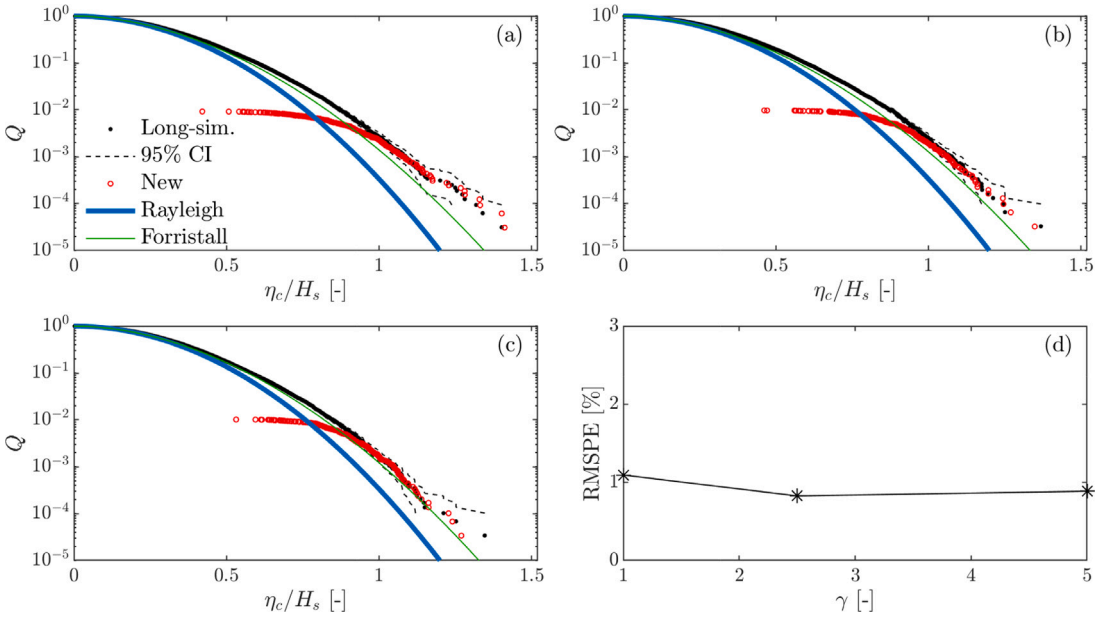

Fig. 14. Measured and predicted $Q(\eta_c)$ in sea states with $H_s = 15$ m, $T_p = 16$ s, $\sigma_\theta = 20°$ and (a) $\gamma = 1.0$, (b) $\gamma = 2.5$ and (c) $\gamma = 5.0$. In part (d) the RMSPEs appropriate to these cases are quantified as described previously for $10^{-3} \geq Q \geq 10^{-4}$. Note: new refers to data collected following the new method.

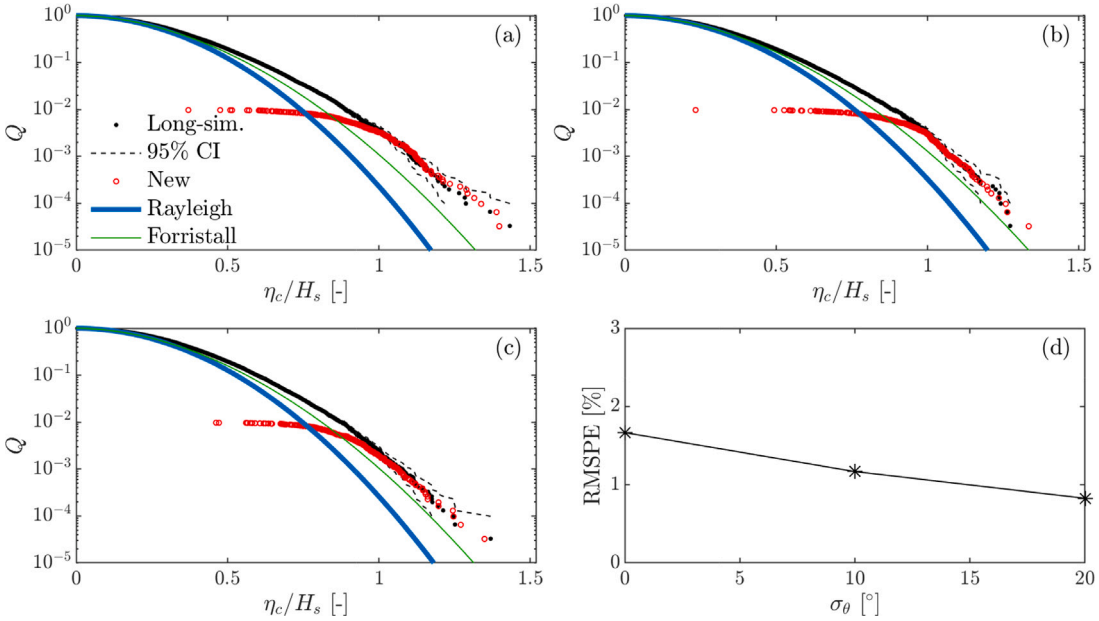

Fig. 15. Measured and predicted $Q(\eta_c)$ in sea states with $H_s = 15$ m, $T_p = 16$ s, $\gamma = 2.5$ and (a) $\sigma_\theta = 0°$, (b) $\sigma_\theta = 10°$ and (c) $\sigma_\theta = 20°$. In part (d) the RMSPEs appropriate to these cases are quantified as described previously, for $10^{-3} \geq Q \geq 10^{-4}$.

Karmpadakis et al. (2019). In the present context it is important to note that this involves a highly optimised procedure in which the use of the wave basin is completely automated and therefore used continuously, except during the essential settling periods. In contrast, the generation of $N = 200$ isolated wave events takes just over 3 h, so a full order of magnitude quicker. Importantly, for exceedance probabilities lying in the range $10^{-3} \geq Q \geq 10^{-4}$, Figs. 14(d) and 15(d) confirm that the *tail* of $Q(\eta_c)$ can be defined with no loss of accuracy; the RMSPE within this range being approximately 1%. The only exception to this occurs in the uni-directional sea state ($\sigma_\theta = 0$ on Fig. 15(a)). In this case both the extent of the downstream shifting and the intensity of wave breaking will be much enhanced, due to increased wave front steepness. Nevertheless, even in this case, the *tail* of the distribution continues to be well described.

6. Predicting confidence intervals

Having established that the *tail* of $Q(\eta_c)$ can be accurately defined using the proposed method, attention must now turn to the definition of the associated confidence intervals, CI. The importance of this interval, particularly when seeking to define the effective reliability of a structure, was addressed in Section 2 and should not be under-estimated. Fig. 16(a) presents data arising from 40 × 3-hour linear simulations of a sea state defined by $H_s = 15$ m, $T_p = 16$ s, $\gamma = 2.5$ and $\sigma_\theta = 15°$. Rather than concatenating the data to explore very small exceedance probabilities, $Q < 10^{-4}$, each of the 40 seeds is used to define a separate distribution, $Q(\eta_c/H_s)$, where Q now lies within the range: $10^0 > Q > 10^{-3}$. The *fan* of data that results is immediately apparent and allows a direct calculation of the CI; the 95% CI being commonly adopted in engineering practice. Although Fig. 16(a) presents data based on linear simulations, related plots could be based on second-order random wave theory (Sharma and Dean, 1981) or fully nonlinear laboratory observations. Figs. 16(b), 16(c) and 16(d) contrast the results arising from these alternative data sets; each of these sub-plots concerning a different sea state steepness. In each case the spread of the data for a given Q is indicative of the CI and quantified by a standard deviation, $\sigma(\eta_c/H_s)$. Fig. 16(b) concerns a near-linear sea state, with steepness $S_p = 0.008$. In this example σ arising from the laboratory data and the second-order calculations are closely aligned and only marginally larger than the linear solution; the difference becoming larger for reducing Q. In contrast, Fig. 16(c) concerns a steeper sea state ($S_p = 0.023$). In this case σ from the second-order calculations is consistently larger than the linear predictions for all $Q \leq 10^{-2}$. Moreover, the laboratory data exhibits a further increase. The explanation for this trend lies in the nonlinear amplification of η_c, first at 2nd-order and then, in respect of the laboratory data, at 3rd-order and beyond. With the nonlinear amplifications depending on wave steepness, but the data ranked in terms of η_c, the wave events corresponding to a given Q will exhibit varying steepness (confirmed in Fig. 3) and hence varying nonlinear amplifications leading to an increase in σ. This pattern is repeated in Fig. 16(d) corresponding to an even steeper sea state ($S_p = 0.038$); the only difference occurring in the very largest events ($Q \approx 10^{-3}$) for which σ from the laboratory data exhibits a marked reduction. This is driven by the dissipative effects of wave breaking, limiting the height of some of the steepest waves and hence reducing σ. Interestingly, for the smallest probability of exceedance ($Q_{\min}$), σ based upon the laboratory data lies below the linear predictions, emphasising the importance of wave breaking.

Figs. 16(e) and (f) provide an alternative view of the same effects. In these cases the σ values are plotted as a function of the sea state steepness, S_p, for $Q = 10^{-2}$ and 10^{-3} respectively. Comparisons between these sub-plots confirm the dissipative effects of wave breaking and the consequent reduction in CI. As expected, the effect is most pronounced in the steepest sea states.

With Fig. 16 having explored potential changes in CI due to the improved physical understanding outlined in Section 2, the question that remains is whether these effects can be predicted based upon the methodology outlined in Sections 3 and 4. Fig. 17(a) defines $Q(\eta_c)$ based upon the concatenation of the 40 × 3-hour of linear simulations of the same sea state as presented in Fig. 16(a). As expected, the resulting data lies very close to the Rayleigh distribution (Eq. (1)), the only departures occurring in the extreme *tail* where CI is largest. Applying a bootstrap analysis (Efron, 1979) allows the data to be re-sampled and the CI estimated. These are shown to be in close agreement with theoretical estimates based upon the assumed Rayleigh distribution following the distribution of ordered statistics (this can be found in standard statistical texts, for example, Casella and Berger, 2002; see also, in the context of ocean waves, Tayfun and Fedele, 2007). Fig. 17(b) shows exactly the same results, but with the exceedance probabilities focused on the *tail* of the distribution ($10^{-3} \geq Q \geq$

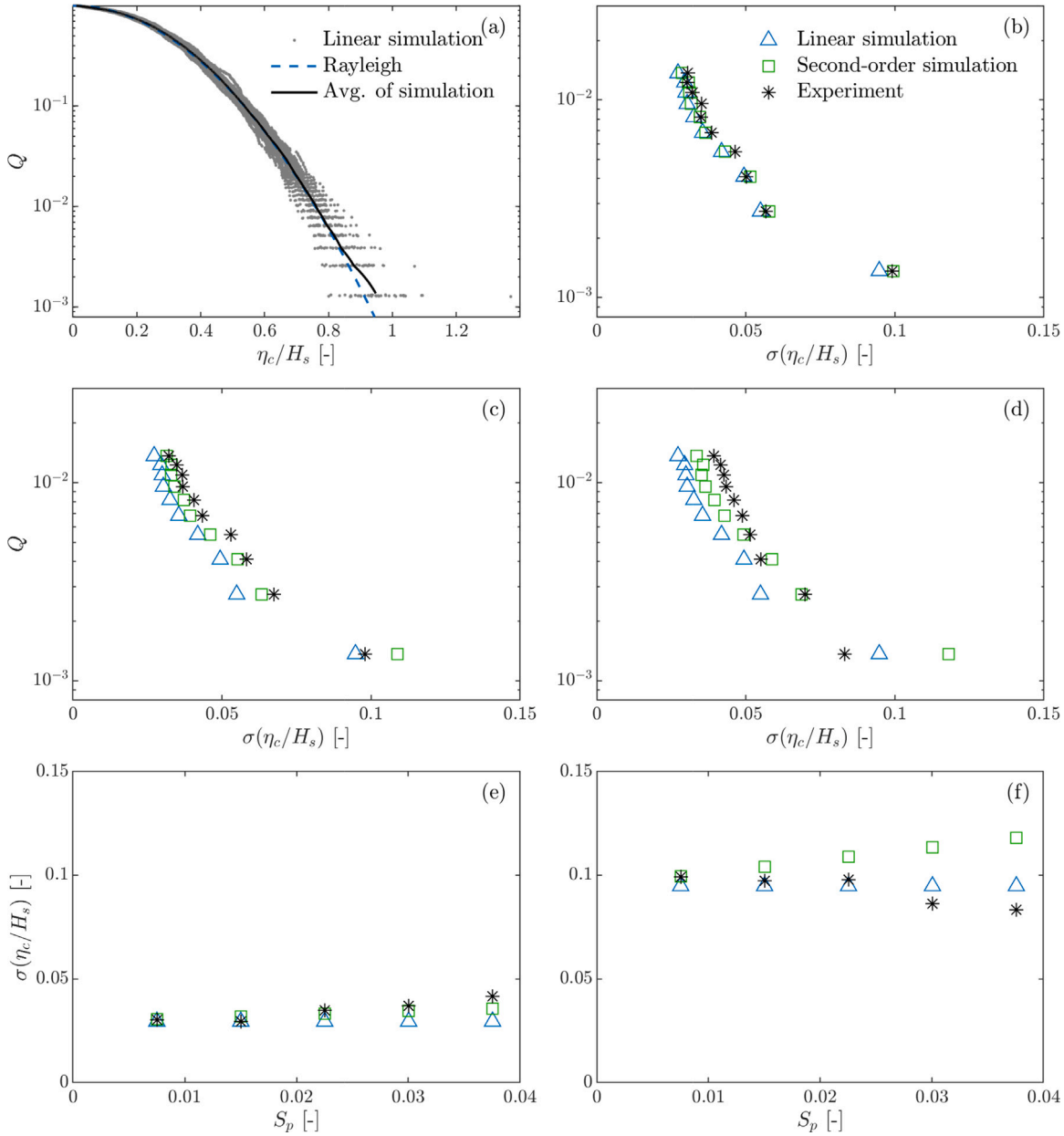

Fig. 16. Nonlinear changes in CI, characterised using the standard deviation, σ, of the crest height distributions arising from multiple seeds. (a) Example data arising from 40 × 3-hour linear simulations. Calculated $\sigma(\eta_c/H_s)$ vs Q for (b) a linear sea state (S_p = 0.008), (c) a nonlinear sea state (S_p = 0.023) and (d) a highly nonlinear sea state (S_p = 0.038) incorporating multiple breaking waves. Calculated $\sigma(\eta_c/H_s)$ vs S_p for (e) $Q = 10^{-2}$ and (f) $Q = 10^{-3}$.

2×10^{-5}). In this figure the only limitation of the bootstrap analysis lies in its inability to predict the upper-bound of the largest values arising at the smallest Q. This is exactly as expected; the method limited by the available data. The obvious remedy for this is to ensure that the available data always extends well beyond the smallest required exceedance probability. Fig. 17(c) again considers a linear simulation of the same sea state, focusing on the range $10^{-3} \geq Q \geq 2 \times 10^{-5}$. In this case comparisons are made between the full 40 × 3-hour long random simulations and the $N = 200$ isolated events generated as deterministic waves using the methodology outlined in Section 3. With all the calculations linear, the correct data points are identified (as explained in Fig. 9(b)) and exactly overlie. The next step involves applying a bootstrap analysis to the $N = 200$ points. Rather than ordering the re-sampled data from smallest to largest η_c, it is reverse-ordered from largest to smallest, assuming the largest η_c in each sample corresponds to the linearly predicted exceedance, $Q_{\min}$. Provided the CIs are only sought over a limited range ($10^{-3} \geq Q \geq 2 \times 10^{-5}$), which lies well within that covered by the $N = 200$ points, the re-sampling will be relevant over the target range and the CIs appropriately defined. The success of this approach is clearly demonstrated in Fig. 17(c); the CIs based upon the long random simulations being closely approximated by the analysis of the $N = 200$ deterministic points. Whilst this is not a formal proof of the appropriateness of the adopted method, it serves as a first example that the CI appropriate to the *tail* of the distribution can also be quantified.

Fig. 17(d) provides a similar plot to Fig. 17(c), addresses a steep sea state, $S_p = 0.038$, defined by $H_s = 15$ m, $T_p = 16$ s, $\gamma = 2.5$ and $\sigma_\theta = 15°$; the 40 × 3-hour of data (indicated in black) based upon laboratory observations. Superimposed upon this data, the red data points correspond to the largest fully nonlinear crests in ranked order from the $N = 200$ events identified from an independent linear analysis (following Section 3) and subsequently regenerated as isolated

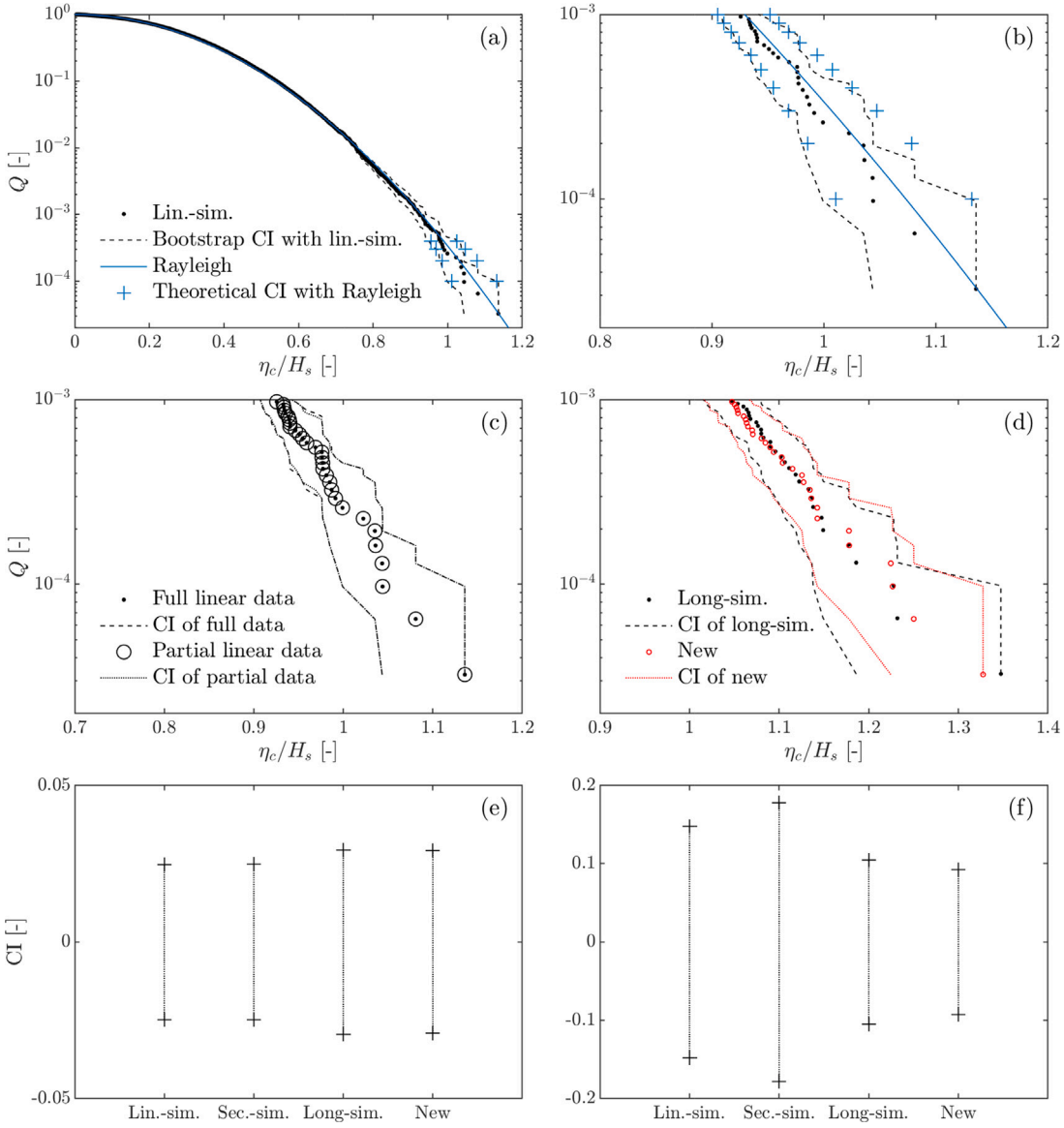

Fig. 17. Estimating CI in the *tail* of the distribution. (a) Example data based upon 40 × 3-hour linear simulations (same sea state as Fig. 16(a)) with comparison to the Rayleigh distribution. (b) Close up of (a) for $10^{-3} \geq Q \geq 2 \times 10^{-5}$. (c) Comparison between full linear simulation and $N = 200$ linear deterministic events. (d) As (c) for a highly non-linear sea state ($S_p = 0.038$) with the traditional long random simulations (denoted by long-sim.) compared with $N = 200$ deterministic events following the new method; and (e), (f) 95% CI at $Q = 10^{-3}$ and $Q = 10^{-4}$, respectively, with comparisons between alternative data sets. Note: lin.-sim. stands for linear simulation, sec.-sim stands for second-order simulation.

deterministic wave events using the parameters discussed in Section 4 (Table 1). Given the success outlined on Figs. 14 and 15, it is not surprising that $Q(\eta_c)$ is well defined. Moreover, given the further success of a bootstrap analysis applied to a truncated data set of $N = 200$ points that are known to populate $Q(\eta_c)$ within the range $10^{-3} \geq Q \geq 2 \times 10^{-5}$ (shown on Fig. 17(c)), it is interesting to note that similar success is achieved in modelling the CI arising in a very steep sea state subject to the combined effects of nonlinear amplification and wave breaking.

The lowermost sub-plots on Fig. 17 contrast the measured and predicted 95% CI based upon linear, second-order and fully nonlinear simulations close to $Q = 10^{-3}$ and 10^{-4} respectively. The first case, Fig. 17(e) shows that the CI increases due to nonlinear amplifications arising both at second-order and above. In contrast, with $Q = 10^{-4}$ on Fig. 17(f) the CI appropriate to the fully nonlinear observations reduce relative to second-order predictions due to the dissipative effects of wave breaking. Importantly, both cases show that the CI can be accurately and efficiently estimated based upon an analysis of $N = 200$ deterministic events.

7. Conclusion

A new method of defining both the *tail* of the short-term crest height distribution, $Q(\eta_c)$, and the associated confidence intervals, CIs, has been outlined. This is based upon a two-stage analysis. First, a relatively small number of extreme wave events are pre-selected from a linear simulation of the target sea state. These events correspond to the largest linearly predicted crest heights arising anywhere over an area positioned immediately upstream of the target location at which point statistics are required. Provided both the area and the number of linear events are sufficiently large (the full details given in Section 3), this set of linearly predicted events will encompass all those events which, after their nonlinear amplification/evolution and the dissipative effects of wave breaking, populate the *tail* of the crest height distribution. The second stage, outlined in Section 4, seeks to incorporate both the full nonlinearity and wave breaking, essentially providing a linear to fully nonlinear transformation of each wave. Within the present paper this is achieved empirically with isolated random waves generated deterministically. The proposed method has been shown to be both accurate and

highly efficient when compared to independent laboratory data arising from very long random wave simulations; the latter covering a broad range of sea states. Importantly, the method concentrates on the largest, and hence the most design-relevant crest heights, avoiding the need to generate the very large number of near-linear waves which form the majority of $Q(\eta_c)$. As such, it is at least an order of magnitude quicker than traditional approaches with no loss of accuracy; the RMSPEs being less than 1% for exceedance probabilities lying in the range $10^{-3} \geq Q \geq 10^{-4}$. This allows the rapid investigation of smaller exceedance probabilities with a consequent reduction in the confidence intervals; the latter defined using standard bootstrap procedures applied to the deterministically generated data. Thus far, the method has been applied to describe the short-term distribution of crest heights, but could easily be adapted to describe the long-term distribution of either crest heights or applied loads. This work is presently on-going, but with long-term distributions involving a summation over all possible sea states, the potential efficiency gains will be further increased with no loss of accuracy. Finally, the transformation of each pre-selected wave event from linear to fully nonlinear is presently undertaken using laboratory observations. With continued improvement in the numerical modelling of breaking waves, future calculations may be achieved without recourse to laboratory observations, giving further substantial efficiency gains; as well as enabling the wider applicability of the method.

CRediT authorship contribution statement

Chong Huo: Methodology, Software, Formal analysis, Investigation, Visualization. **Chris Swan:** Conceptualization, Writing – original draft, Writing – review & editing, Supervision. **Ioannis Karmpadakis:** Writing – review & editing, Resources. **Li Ma:** Writing – review & editing, Resources.

Declaration of competing interest

The authors declare that they have no known competing financial interests or personal relationships that could have appeared to influence the work reported in this paper.

Data availability

The authors are unable or have chosen not to specify which data has been used.

References

Adcock, T.A., Taylor, P.H., Draper, S., 2015. Nonlinear dynamics of wave-groups in random seas: Unexpected walls of water in the open ocean. Proc. R. Soc. A 471 (2184), http://dx.doi.org/10.1098/rspa.2015.0660.

API, 2014. Structural Integrity Management of Fixed Offshore Structures API Recommended Practice 2SIM. American Petroleum Institute (API), Washington D.C.

Baldock, T.E., Swan, C., Taylor, P.H., 1996. A laboratory study of nonlinear surface waves on water. Phil. Trans. R. Soc. A 354 (1707), 650–675. http://dx.doi.org/10.1098/rsta.1996.0022.

Benjamin, T.B., Feir, J.E., 1967. The disintegration of wave trains on deep water Part 1. Theory. J. Fluid Mech. 27 (3), 417–430. http://dx.doi.org/10.1017/S002211206700045X, URL https://www.cambridge.org/core/product/identifier/S002211206700045X/type/journal_article.

Boccotti, P., 1983. Some new results on statistical properties of wind waves. Appl. Ocean Res. 5 (3), 134–140. http://dx.doi.org/10.1016/0141-1187(83)90067-6.

Casella, G., Berger, R., 2002. Statistical Inference. Duxbury Resource Center.

Chabchoub, A., Hoffmann, N., Akhmediev, N., 2011. Rogue wave observation in a water wave tank. Phys. Rev. Lett. 106, 204502. http://dx.doi.org/10.1103/PhysRevLett.106.204502, URL https://link.aps.org/doi/10.1103/PhysRevLett.106.204502.

Dean, R., 1970. Relative validities of water wave theories. J. Waterw. Harb. Coast. Eng. Div. 96, 105–119. http://dx.doi.org/10.1061/AWHCAR.0000003.

DNV-GL, 2019. Recommended Practice DNVGL-RP-C205: Environmental Conditions and Environmental Loads. DNV-GL, Norway, p. 40.

Efron, B., 1979. Bootstrap methods : Another look at the jackknife. Ann. Statist. 7 (1), 1–26.

Fedele, F., Brennan, J., Ponce De León, S., Dudley, J., Dias, F., 2016. Real world ocean rogue waves explained without the modulational instability. Sci. Rep. 6 (June), 1–11. http://dx.doi.org/10.1038/srep27715.

Fedele, F., Herterich, J., Tayfun, A., Dias, F., 2019. Large nearshore storm waves off the Irish coast. Sci. Rep. 9 (1), 1–19. http://dx.doi.org/10.1038/s41598-019-51706-8.

Fedele, F., Tayfun, M.A., 2009. On nonlinear wave groups and crest statistics. J. Fluid Mech. 620, 221–239. http://dx.doi.org/10.1017/S0022112008004424.

Forristall, G.Z., 2000. Wave crest distributions: Observations and second-order theory. J. Phys. Oceanogr. 30 (8), 1931–1943. http://dx.doi.org/10.1175/1520-0485(2000)030<1931:WCDOAS>2.0.CO;2.

Gibson, R.S., Swan, C., 2007. The evolution of large ocean waves: The role of local and rapid spectral changes. Proc. R. Soc. A 463 (2077), 21–48. http://dx.doi.org/10.1098/rspa.2006.1729.

Hasselmann, K., 1962. On the non-linear energy transfer in a gravity-wave spectrum Part 1. General theory. J. Fluid Mech. 12 (4), 481–500.

ISO, 2013. Petroleum and Natural Gas Industries — Fixed Steel Offshore Structures (ISO 19902:2007/Amd.1:2013). International Organization for Standardization (ISO), URL https://www.iso.org/standard/27507.html.

Jacobsen, N., Fuhrman, D., Fredsøe, J., 2012. A wave generation toolbox for the open-source CFD library: OpenFoam®. Int. J. Numer. Methods Fluids 70, 1073–1088. http://dx.doi.org/10.1002/fld.2726.

Janssen, P., 2003. Nonlinear four-wave interactions and freak waves. J. Phys. Oceanogr. 33, 863–884. http://dx.doi.org/10.1175/1520-0485(2003)33<863:NFIAFW>2.0.CO;2.

Johannessen, T.B., Swan, C., 2001. A laboratory study of the focusing of transient and directionally spread surface water waves. Proc. R. Soc. A 457 (2008), 971–1006. http://dx.doi.org/10.1098/rspa.2000.0702.

Johannessen, T.B., Swan, C., 2003. On the nonlinear dynamics of wave groups produced by the focusing of surface-water waves. Proc. R. Soc. A 459 (2032), 1021–1052. http://dx.doi.org/10.1098/rspa.2002.1028.

Karmpadakis, I., Swan, C., 2020. On the average shape of the largest waves in finite water depths. J. Phys. Oceanogr. 50, 1023–1043. http://dx.doi.org/10.1175/JPO-D-19-0165.1.

Karmpadakis, I., Swan, C., 2022. A new crest height distribution for nonlinear and breaking waves in varying water depths. Ocean Eng. 266 (4), http://dx.doi.org/10.1016/j.oceaneng.2022.112972.

Karmpadakis, I., Swan, C., Christou, M., 2019. Laboratory investigation of crest height statistics in intermediate water depths. Proc. R. Soc. A 475 (2229), http://dx.doi.org/10.1098/rspa.2019.0183.

Kharif, C., Pelinovsky, E., 2003. Physical mechanisms of the rogue wave phenomenon. Eur. J. Mech. B 22, 603–634. http://dx.doi.org/10.1016/j.euromechflu.2003.09.002.

Latheef, M., Swan, C., 2013. A laboratory study of wave crest statistics and the role of directional spreading. Proc. R. Soc. A 469 (2152), http://dx.doi.org/10.1098/rspa.2012.0696.

Latheef, M., Swan, C., Spinneken, J., 2017. A laboratory study of nonlinear changes in the directionality of extreme seas. Proc. R. Soc. A 473 (2199), http://dx.doi.org/10.1098/rspa.2016.0290.

Le Méhauté, B., 1976. An introduction to hydrodynamics and water waves. Springer, Berlin.

Lindgren, G., 1970. Some properties of a normal process near a local maximum. Ann. Math. Stat. 41 (6), 1870–1883. http://dx.doi.org/10.1214/aoms/1177696688.

Longuet-Higgins, M.S., 1952. On the statistical distribution of the heights of sea waves. J. Mar. Res. 11 (5), 245–266.

Ma, L., 2017. The Effective Modelling of Wave-in-deck Loads (Ph.D. thesis). Imperial College London.

Ma, L., Swan, C., 2023. Wave-in-deck loads: an assessment of present design practice given recent improvements in the description of extreme waves and the nature of the applied loads. Ocean Engineering 285, 115302. http://dx.doi.org/10.1016/j.oceaneng.2023.115302.

NORSOK, 2017. N-003 actions and action effects, third ed. Norwegian Technology Standards Institution (NORSOK), Oslo, Norway.

Phillips, O.M., Gu, D., Donelan, M., 1993a. Expected structure of extreme waves in a Gaussian Sea. Part I: Theory and SWADE buoy measurements. J. Phys. Oceanogr. (5), 992–1000.

Phillips, O.M., Gu, D., Walsh, E.J., 1993b. On the expected structure of extreme waves in a Gaussian Sea. Part II: SWADE scanning radar altimeter measurements. J. Phys. Oceanogr. (10), 2297–2309.

Schubert, M., Wu, Y., Tychsen, J., Dixen, M., Faber, M.H., Sørensen, J.D., Jonathan, P., 2020. On the distribution of maximum crest and wave height at intermediate water depths. Ocean Eng. 217 (May), http://dx.doi.org/10.1016/j.oceaneng.2020.107485.

Sharma, J., Dean, R., 1981. Second-order directional seas and associated wave forces. Soc. Petrol. Eng. 4, 129–140.

Sobey, R., Goodwin, P., Thieke, R., J. Westberg Jr., R., 1987. J. Water. Port, Coast. Ocean Eng. 113, 565–587.

Spinneken, J., Swan, C., 2009a. Second-order wave maker theory using force-feedback control. Part I: A new theory for regular wave generation. Ocean Eng. 36 (8), 539–548.

Spinneken, J., Swan, C., 2009b. Second-order wave maker theory using force-feedback control. Part II: An experimental verification of regular wave generation. Ocean Eng. 36 (8), 549–555.

Swan, C., Gibson, R.S., 2018. Extreme Environmental Loading of Fixed Offshore Structures. Technical Report October, HSE, URL https://www.hse.gov.uk/offshore/research/extreme-wave.htm.

Tayfun, M.A., 1994. Distributions of envelope and phase in weakly nonlinear random waves. J. Phys. Oceanogr. 120 (4).

Tayfun, M.A., 2006. Statistics of nonlinear wave crests and groups. Ocean Eng. 33 (11–12), 1589–1622. http://dx.doi.org/10.1016/j.oceaneng.2005.10.007.

Tayfun, M., Fedele, F., 2007. Wave-height distributions and nonlinear effects. Ocean Eng. 34, 1631–1649. http://dx.doi.org/10.1016/j.oceaneng.2006.11.006.

Tucker, M.J., Pitt, E.G., 2001. Waves in Ocean Engineering. In: Elsevier Ocean Engineering Book Series, vol. 5, Elsevier, Amsterdam.

Tychsen, J., Risvig, S., Hansen, H., Hansen, N.-E.O., Stevanato, F., 2016. Summary of the impact on structural reliability of the findings of the tyra field extreme wave study 2013-15. In: 3rd Offshore Structural Reliability Conference. pp. 14–16.